Catalysis Science & Technology

First-principles microkinetic modeling of partial methane oxidation over graphene-stabilized single-atom Fe-catalysts

Journal:	*Catalysis Science & Technology*
Manuscript ID	CY-ART-09-2023-001335.R1
Article Type:	Paper
Date Submitted by the Author:	07-Nov-2023
Complete List of Authors:	Hong, Sungil; University of Pittsburgh, Chemical Engineering Kauppinen, Minttu Maria; Chalmers University of Technology, Physics Miu, Evan; University of Pittsburgh, Chemical and Petroleum Engineering Mpourmpakis, Giannis; University of Pittsburgh, Chemical and Petroleum Engineering Groenbeck, Henrik; Chalmers University of Technology, Physics

ARTICLE

First-principles microkinetic modeling of partial methane oxidation over graphene-stabilized single-atom Fe-catalysts

Received 00th January 20xx,
Accepted 00th January 20xx

DOI: 10.1039/x0xx00000x

Sungil Hong,[a] Minttu M. Kauppinen,[b] Evan V. Miu,[a] Giannis Mpourmpakis*[a] and Henrik Grönbeck*[b]

Catalytic conversion of CH_4 to transportable liquid hydrocarbons via partial oxidation is a promising avenue towards efficient utilization of natural gas. Single Fe atoms on N-functionalized graphene (FeN_4/GN) have recently been shown to be active for partial CH_4 oxidation with H_2O_2 at room temperature. Here, density functional theory (DFT) calculations combined with mean-field microkinetic modeling (MKM) have been applied to obtain kinetic understanding of partial CH_4 oxidation with H_2O_2 to CH_3OH and CH_3OOH over FeN_4/GN. CH_3OH and CH_3OOH are found to be minor and major reaction products, respectively, with a selectivity in agreement with reported experimental data. The kinetic modeling reveals two pathways for CH_3OH production together with a dominant catalytic cycle for CH_3OOH formation. The selectivity is found to be sensitive to the temperature and H_2O_2 concentration, with the CH_3OH selectivity increasing with increasing temperature and decreasing H_2O_2 concentration. Turnover frequencies of both CH_3OH and CH_3OOH are found to decrease over time, due to a change in the Fe formal oxidation state from +6 to +4; Fe(+6) is more active, but less stable than Fe(+4). The present work unravels the detailed reaction mechanism for partial oxidation of methane by FeN_4/GN, rationalizes experimental observations and provides guidance for efficient room-temperature methane conversion by single-atom Fe-catalysts.

Introduction

Natural gas is still one of the most important energy sources.[1] The share of natural gas in global energy production has gradually increased over the last decade due to its vast reserves and less CO_2 released per produced energy unit compared to other fossil fuels.[1,2] Nevertheless, natural gas associated with petroleum extraction has been flared since its utilization is not profitable and CH_4 (the largest component of natural gas) has a much higher global warming potential than CO_2.[3] The amount of natural gas flared worldwide is as much as 17% of the total natural gas consumption in the United States.[1,4] CH_4 is flared because of challenges handling gaseous products at the sites of petroleum extraction and the lack of processes for small scale on-site catalytic conversion to liquid products. The commercial CH_4-to-CH_3OH conversion process is presently syngas production followed by Fischer-Tropsch synthesis, which are highly centralized and energy intensive processes.[5-7]

Small-scale on-site catalytic conversion of CH_4 to liquid hydrocarbon could be a promising avenue toward valorizing natural gas that presently is being wasted. The liquid derivatives of CH_4 can replace natural gas as a primary energy source since the storage and transportation of liquid products are safer and less costly than those of gaseous products. Further, the possible products, e.g., alcohols and olefins, are value-added chemicals with high industrial demand. Especially, methanol (CH_3OH) is a valuable target chemical, since it can be used as both a fuel for combustion engines[8] or fuel cells,[9,10] and chemical feedstock for a range of chemicals, such as methyl tertiary-butyl ether,[11] dimethyl ether,[12] and formaldehyde[13]. Hence, significant research has been recently devoted to study catalysts for direct partial CH_4 oxidation at low temperatures. Direct partial oxidation of CH_4 is challenging due to the chemical inertness of CH_4.[14] High temperatures facilitate C−H bond activation, but with the risk of over-oxidation of CH_3OH to CO_2, as the C−H bond of CH_3OH is weaker than that of CH_4.[14,15] Thus, CH_4-to-CH_3OH conversion should be performed at low temperatures. Over-oxidation could be suppressed by having well-defined catalytic sites with single metal centers embedded in an inert matrix. However, single metal centers may not be multifunctional and active for O_2 activation (in addition to CH_4 activation), requiring oxidants such as N_2O and H_2O_2.[16]

Metal- and metal oxide-based homogeneous catalysis for CH_4 activation has been widely studied since the 1980s.[17-23] Among many catalysts, CoO^+ and FeO^+ showed activity toward CH_4-to-CH_3OH conversion.[18,19] Periana and coworkers demonstrated high activity of Hg(II) and Pt(II) salts in a concentrated H_2SO_4 solution.[24,25] Moreover, partial oxidation of CH_4 can be performed over methane monooxygenases (MMOs) at room-temperature.[26-29] Despite the partial successes, homogeneous catalysis has intrinsic constraints for commercialization as it requires additional product separation processes, which has motivated research efforts in developing heterogeneous catalysts for CH_4 conversion. Especially, biomimetic partial oxidation of CH_4 using Fe- and Cu-based

[a] Department of Chemical & Petroleum Engineering, University of Pittsburgh, Pittsburgh, Pennsylvania 15261, USA.
[b] Department of Physics and Competence Centre for Catalysis, Chalmers University of Technology, SE-412 96 Göteborg, Sweden.
Emails: gmpourmp@pitt.edu, ghj@chalmers.se
†Electronic supplementary information (ESI) available. See DOI: 10.1039/x0xx00000x

zeolite catalysts has attracted interest. The Fe sites of Fe-ZSM-5 obtain active oxygen species (α-oxygen) from nitrous oxide (N_2O), which can convert CH_4 to CH_3OH.[30-32] The active bi-nuclear Fe center of Fe-ZSM-5 resembles the di-iron center of soluble-MMO enzymes.[30-32] Likewise, Cu-ZSM-5 catalysts have shown activity towards CH_4-to-CH_3OH conversion, mimicking particulate-MMO enzymatic systems, although the nature of the active centers has not been completely understood.[33-35] One severe drawback of the zeolite-based catalysts is that they require elevated temperatures (≥ 200 °C) for the extraction of CH_3OH due to the hydrophilic nature of the zeolite framework.[33,36]

In 2018, Cui and coworkers reported room-temperature activity for partial CH_4 oxidation over N-functionalized single Fe atom catalyst stabilized on graphene (FeN_4/GN) with H_2O_2 as oxidant.[37] The measured reaction products included CH_3OH, CH_3OOH, $HOCH_2OOH$, and HCOOH, where the two last species were suggested to originate from CH_3OH oxidation.[37] Over-oxidation of the reaction product to CO_2 was significantly suppressed probably owing to the low operating temperature (25 °C) and the isolated nature of the active center (6.3% selectivity for CO_2).[37] The CH_4 conversion is comparable to, or higher than, that of zeolite-based catalysts operated at higher temperatures.[38,39]

We have previously performed Density Functional Theory (DFT) calculations to elucidate the reaction paths for partial CH_4 oxidation over FeN_4/GN.[40] Plausible reaction mechanisms were identified that demonstrated the role of H_2O_2 as a key reacting species to produce CH_3OH.[40] Moreover, the Energetic span model proposed by Kozuch and Shaik[41] was applied to estimate the turnover frequencies (TOFs) of different reaction pathways and get activity trends from individual reaction mechanisms. However, the Energetic span model is an over-simplification in this case as it does not account for nested reaction paths and, moreover, does not properly account for the operating conditions, e.g., the reactant concentrations. In addition, our previous work focused primarily on mechanisms producing CH_3OH without considering other products.[40]

Herein, we develop a first-principles-based mean-field microkinetic model (MKM) for CH_4 conversion on FeN_4/GN catalyst. First-principles-based MKM is a powerful tool to provide unbiased kinetic information on TOF, selectivity, apparent activation energy, reaction-orders, surface coverages and rate-controlling reaction steps over a variety of complicated heterogeneous catalytic systems.[42-49] The multiple reaction mechanisms determined using the DFT calculations are coupled in the MKM to examine the kinetic properties of nested catalytic cycles with a dynamic change in the Fe oxidation state.[40] Moreover, to compare with experiments, additional reaction mechanisms for the conversion of CH_4 to methyl hydroperoxide (CH_3OOH), which is another major reaction product[37], have been investigated with DFT and included in the kinetic modeling. The present first-principles-based MKM rationalizes experimental observations, demonstrating the capability of MKM to model a highly complex reaction network and provide a fundamental understanding of the active nature of FeN_4/GN catalyst. This work can guide further efforts on designing efficient catalysts for CH_4 conversion to value-added fuels and chemicals.

Computational details

Density functional theory calculations

Density functional theory (DFT) calculations were performed with the Gaussian 09 software package at the B3LYP/6-31G(d) level of theory.[50-52] Comparative computations with the M06-2X functional yields similar results.[40] Vibrational frequency calculations were performed to confirm that the stationary points are either minima or saddle points. The optimized transition state (TS) structures were confirmed to connect the corresponding reactants and products by Intrinsic Reaction Coordinate calculations[53]. FeN_4/GN is modeled having a central single Fe atom, which is anchored by 4 N atoms to a graphene flake (represented by 26 C atoms terminated by H atoms on the edges). The reaction energetics depend very weakly on the size of the graphene flake (Figure S1). Two different types of active centers were considered[40]: singly oxygenated (mono-oxo) and doubly oxygenated (di-oxo) centers (Figure 1). As the reaction takes place in water experimentally,[37] solvent effects were considered in all calculations by applying the conductor-like polarizable continuum model (CPCM)[54] with water as the solvent. The reaction energetics were described in terms of Gibbs free energy at 298.15 K and 1 atm, unless otherwise specified in the results. The enthalpic and entropic contributions to Gibbs free energy of reaction are assumed to be constant within the small temperature range considered (278.15 - 318.15 K). Hence, Gibbs free energy of reaction at temperature T was calculated as:

$$\Delta G_{rxn,\ T} = \Delta H_{rxn,\ 298.15\,K} - T * \Delta S_{rxn,\ 298.15\,K} \#(1)$$

Entropy values reported in ref.[55] (at 298.15 K in water) were used for all the molecules except CH_3OOH, which is unavailable in the literature. The entropy of CH_3OOH was therefore determined by multiplying a factor of 0.62 to the gas-phase DFT-determined entropy, based on the simple scaling relation reported in Ref.[56] This scaling factor is very similar to how the experimental and gas-phase calculated entropies of H_2O_2 scale (Table S1), demonstrating the validity of this selection considering the structural similarity between the CH_3OOH and H_2O_2 molecules. For the structures involving the catalyst surfaces, real vibrational frequencies lower than 100 cm^{-1} were replaced by 100 cm^{-1} when determining entropies and free energies to reduce errors that can emerge from calculations of low-frequency modes.[57] The studied mechanisms are presented in Figure 2 (*vide infra*) and in Section 2 of the Supplementary Information file.

Microkinetic model

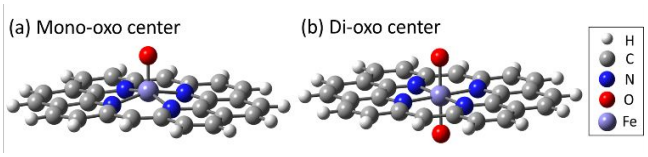

Figure 1 Catalyst structures with (a) mono-oxo and (b) di-oxo FeN_4/GN centers.

The microkinetic model consists of a system of coupled ordinary differential equations, which describe the time-evolution of the concentration of species. The differential equations have the form:

$$\frac{dc_i}{dt} = \sum_j \nu_{ij}\, r_j(\vec{c})\ \#(2)$$

where c_i is the concentration of species i, r_j is the rate of reaction j, which is a function of concentrations $\vec{c}$, and ν_{ij} is the stoichiometric number of species i in reaction j. For the FeN_4/GN system, 'species' are unique complexes between the Fe-center and some (or none) ligands, which include a single oxygen (mono-oxo center), two oxygens (di-oxo center) and other ligands that appear as intermediates in catalytic cycles. The di-oxo center has an initial concentration of unity as it has been suggested to be an active center.[37] The fraction (coverage) of species i (x_i) is defined as the ratio of the number of species i (n_i) to the total number of all the possible species:

$$x_i = \frac{n_i}{\sum_i n_i}\#(3)$$

The mole fractions of all species obey the summation:

$$\sum_i x_i = 1\#(4)$$

In the case of FeN_4/GN, the entire catalytic cycle is assumed to take place at single Fe-centers, with no interaction or cross-reactions between adjacent Fe-centers. Thus, each elementary reaction is first order, with the forward (backward) reaction rate depending only on the concentration of the reactant (product) species multiplied by the rate constant. The rate constants of reactions are calculated according to transition-state theory as:

$$k = \frac{k_B T}{h}\exp\left[-\frac{\Delta G^{\ddagger}}{k_B T}\right]\#(5)$$

where k_B is the Boltzmann constant, T is the temperature, and $\Delta G^{\ddagger}$ is the standard Gibbs free energy barrier determined using DFT calculations as previously described.

Adsorption of a free species (e.g., CH_4 and H_2O_2) from the solution to the catalyst surface is taken to be purely diffusion-controlled, where the catalyst is assumed to be a stationary 2-D flake, giving the following expression for the adsorption rate constant k_a:[58]

$$k_a = 4 r_a D_i c_i\#(6)$$

where r_a is the radius of the active site, and D_i and c_i are the diffusivity and the bulk concentration of the adsorbing species i, respectively. The diffusivity of a free species is obtained by the Stokes-Einstein equation:

$$D_i = \frac{k_B T}{6\pi\eta r_i}\#(7)$$

where η is the viscosity of the fluid and r_i is the radius of the species. The viscosity of the fluid is approximated by the dynamic viscosity of water at room temperature. The relative radius of the adsorption center of the catalyst to free species is approximated to be 4 (i.e., $r_a = 4r_i$), considering the larger size of the FeN_4 center compared to free molecules. This leads to the adsorption rate constant given by:

$$k_a = \frac{8\ k_B T}{3\pi\ \ \eta} c_i\#(8)$$

Note that the unit of k_a is s^{-1}. The desorption rate constants k_d are calculated from the adsorption rate constant via the equilibrium constant K_{eq}:

$$K_{eq} = \frac{k_a}{k_d} = \exp\left[-\frac{\Delta G}{k_B T}\right]\#(9)$$

ΔG is the free energy change of adsorption. Solving eqn. 9 for k_d gives:

$$k_d = k_a \exp\left[\frac{\Delta G}{k_B T}\right]\#(10)$$

Note that k_d (unit s^{-1}) is independent of the bulk concentration of the desorbing species.

The coupled ODEs were solved using a Python 3-based code with the solve_ivp function from the Scipy package[59] scipy.integrate. The integration intervals were chosen to be long enough (10^4 seconds in general) to ensure that a steady state is reached.

Degree of rate control (DRC) and degree of selectivity control (DSC) analyses[60] were performed to identify elementary steps with rate control of the CH_3OH and CH_3OOH formation and the CH_3OH selectivity. DRC of elementary step i ($X_{RC,i}$) is defined as:

$$X_{RC,i} = \frac{k_i}{r}\left(\frac{\partial r}{\partial k_i}\right)_{k_{j\neq i}, K_i}\#(11)$$

where k_i is the forward rate constant of step i and r is the overall reaction rate. The $X_{RC,i}$ is approximated with a finite difference method, performed by lowering the forward and backward rate constant of a single elementary step by 1%, while all the other rate constants k_i are unvaried, and observing the change in the overall reaction rate at steady state. A positive $X_{RC,i}$ value indicates a rate-limiting step, whereas a negative value indicates an inhibition step.[60] The degree of selectivity control $X_{SC,i}$ of an elementary step i is defined as:

Table 1 Reaction conditions and parameters for microkinetic modeling.

Parameter	Symbol	Value	Units
Standard molarity	c°	1	mol·dm^{-3}
H_2O_2 concentration†	$[H_2O_2]$	5	mol·dm^{-3}
H_2O concentration	$[H_2O]$	50	mol·dm^{-3}
CH_4 concentration†	$[CH_4]$	0.03	mol·dm^{-3}
CH_3OH concentration	$[CH_3OH]$	1e-5	mol·dm^{-3}
CH_3OOH concentration	$[CH_3OOH]$	1e-5	mol·dm^{-3}
Dynamic viscosity of water	η	890.2[61]	μPa·s
Henry's constant of CH_4 in water	H_{CH_4}	38741[62]	bar

†Based on the experimental condition[37]

$$X_{SC,i} = \frac{1}{S}\left(\frac{\partial S}{\partial k_i}\right)_{k_{j\neq i}, K_i} \#(12)$$

where S is the CH_3OH selectivity, which is defined as the ratio of the catalyst's TOF to CH_3OH to the sum of the TOFs to both products.

The reaction orders of CH_3OH and CH_3OOH formation were determined with respect to each reactant (CH_4 and H_2O_2) as calculated from:

$$n_i = \frac{\partial \ln r}{\partial \ln c_i} \#(13)$$

where r is the net reaction rate and c_i is the concentration of the reactant i. The partial derivatives were approximated by finite differences by increasing c_i by 1%, while all the other parameters were kept constant. Apparent activation energies for CH_3OH and CH_3OOH formation were calculated from the slopes of their respective Arrhenius plots in the temperature range from 278.15 to 318.15 K. This approach is valid as the plots were found to be linear in the tested temperature range. Reaction conditions and parameters used in the MKM are listed in Table 1.

Further details on MKM can be found in the Supplementary Information Section 3 and the assumptions made in the diffusion model are discussed in the Supplementary Information Section 4.

Results and discussion

Methane conversion mechanisms

CH_3OH formation. Prior work[40] identified 11 different mechanisms of CH_4-to-CH_3OH conversion over FeN_4/GN. Gibbs free energy profiles of some relevant pathways are reproduced here (Figures 2, S1, and S2) for completeness and as additional corrections have been made to the Gibbs free energies for higher accuracy (see Computational details). Figure 2a and b shows two important mechanisms for CH_4-to-CH_3OH conversion with the net reaction:

$$CH_4 + H_2O_2 \rightarrow CH_3OH + H_2O \ \#(rxn.1)$$

Path 1 proceeds over the di-oxo species and is an H_2O_2-mediated radical mechanism (Figure 2a). The di-oxo center breaks a primary C−H bond of CH_4 to generate a methyl radical ($CH_3\cdot$), which reacts with H_2O_2 to give CH_3OH and a hydroxyl radical ($OH\cdot$). Thereafter, the hydroxyl radical abstracts H from the hydroxyl center to regenerate the di-oxo-center. Path 2 proceeds over the mono-oxo species and is a Fenton-type reaction mechanism (Figure 2b). The O=O bond of H_2O_2 is in this case homolytically dissociated at the bare Fe side of the mono-oxo center (bottom of the structure shown in Figure 1(a)), producing a hydroxyl radical and hydroxylating the Fe site. The hydroxyl radical activates CH_4 to $CH_3\cdot$, which is converted to CH_3OH by abstracting the hydroxyl surface ligand.

Additional mechanisms include one on a di-oxo center (direct radical mechanism as path 4; Figure S2) and two on a mono-oxo center (direct and H_2O_2-mediated radical mechanisms as path 5 and 6, respectively; Figure S3). These pathways are associated with higher barriers either for the recovery of the active center (path 4) or homolytic C-H dissociation of CH_4 (paths 5 and 6). Importantly, the different reaction mechanisms share some common states. For example, Paths 1 and 2 have common state 3 (Figure 2), which suggests a possibility of a larger reaction network with a dynamic oxidation state of Fe along the reaction coordinate.

CH_3OOH formation. CH_3OOH is another major, experimentally observed, reaction product.[37] Thus, we examine reaction mechanisms for CH_4 conversion to CH_3OOH on both the di-oxo (Path 3 in Figure 2) and mono-oxo (Path 7 in Figure S3) centers. The four first elementary steps of path 3 are identical to those in Path 1; the di-oxo center homolytically dissociates the primary C−H bond of CH_4, and one H_2O_2 is adsorbed on the surface. Thereafter, one H from H_2O_2 is abstracted by the hydroxylated center, and $CH_3\cdot$ species is combined with the remaining $\cdot OOH$ simultaneously, producing surface water and CH_3OOH (TS7). This radical mechanism resembles the CH_4 conversion by Pd/MoO_3 photocatalyst reported in Ref.[63] Next the surface water is dehydrogenated (to OH) by a second H_2O_2, producing one water molecule and a hydroxyl radical ($OH\cdot$) as the O=O bond of H_2O_2 is dissociated (TS8). This step involves the highest activation energy in the pathway ($\boldsymbol{\Delta G}^{\ddagger}$ = 1.00 eV). The remaining hydroxyl center is further dehydrogenated by $OH\cdot$, regenerating the di-oxo active center and closing the catalytic cycle. The mono-oxo counterpart of path 3 is path 7 in Figure S3, which involves a high activation energy for the C−H bond cleavage (TS10, $\boldsymbol{\Delta G}^{\ddagger}$ = 1.52 eV). Hence, substantial formation of CH_3OOH is only possible via path 3. The net reaction of the mechanism for this reaction is:

$$CH_4 + 2H_2O_2 \rightarrow CH_3OOH + 2H_2O \ \#(rxn.2)$$

There are two important observations on Path 3: First, TS7 (producing CH_3OOH) competes with TS2 of path 1 (producing CH_3OH) since they share the reactant state (state 4), where the barrier for CH_3OOH formation is lower than that of CH_3OH formation, which indicates a preference for CH_3OOH formation over the di-oxo center. Second, state 15 (after CH_3OOH has desorbed) is essentially a mono-oxo center with a water molecule on the bare Fe side. If the water desorbs (instead of going through the remaining steps in path 3), then the system is converted to the bare mono-oxo state (state 8). Conversely, if one water molecule adsorbs on the bare Fe site of the

mono-oxo catalyst and reacts with H_2O_2 (through TS8), it forms the di-oxo center. These scenarios provide routes to connect different reaction mechanisms on two different active centers. To investigate the possibility of dynamic behavior of the active center, the additional elementary step of water adsorption on the bare Fe site of the mono-oxo center is considered in the MKM.

Microkinetic modeling

Reaction network. We carried out MKM calculations with the parameters in Table 1 using either the full reaction mechanism or a reduced set of the reaction mechanisms. For the full reaction mechanism, all the reaction pathways on both the di- and mono-oxo centers (i.e., paths 1-7) are considered. For the reduced set of reaction mechanisms, only three energetically feasible mechanisms (i.e., paths 1-3) were included. The differences of the total TOFs between the full reaction mechanisms and the reduced set of the reaction mechanisms are negligible owing to the high barriers in paths 4-7 (see

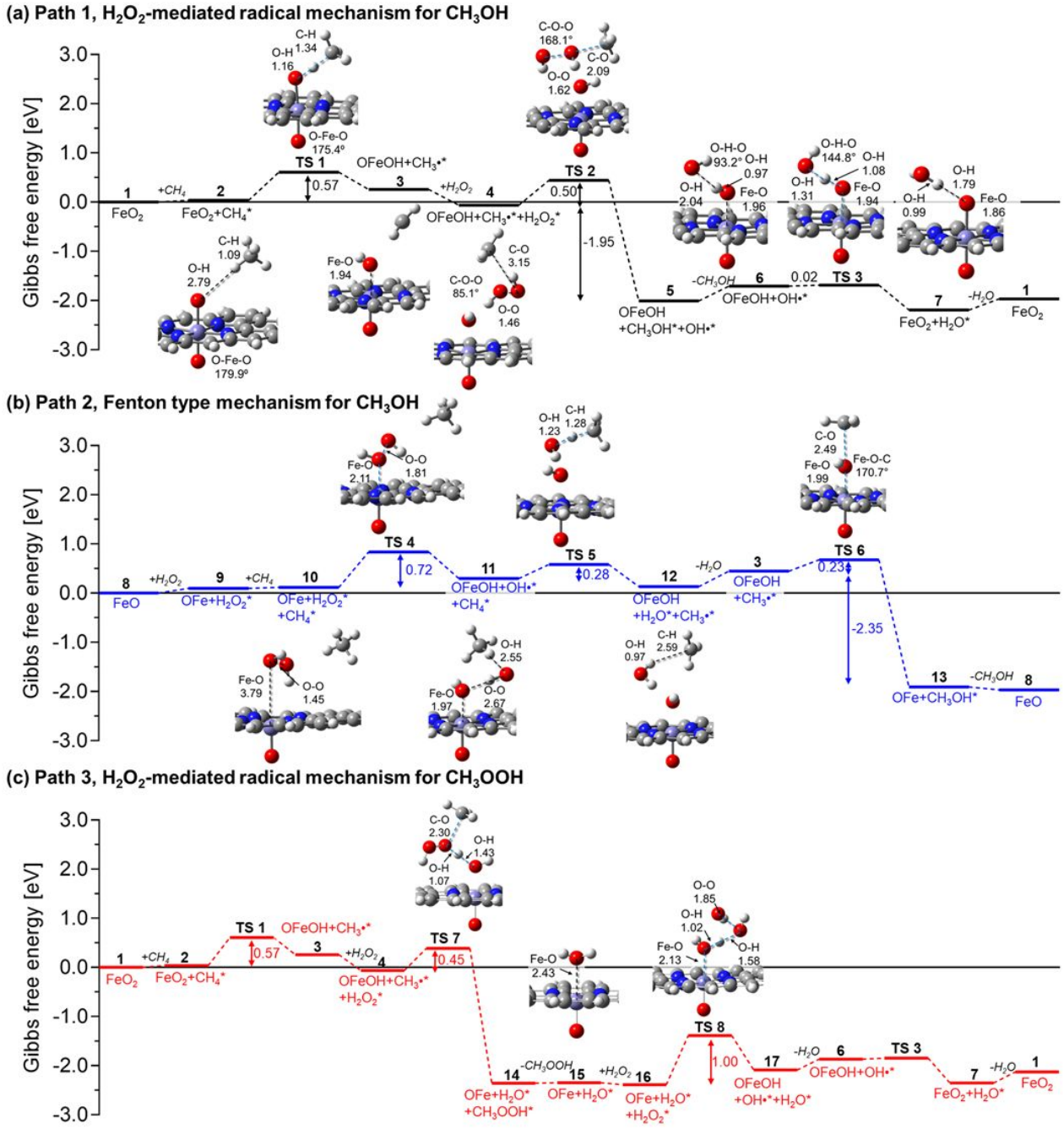

Figure 2 Detailed Gibbs free energy profiles of CH_4-to-CH_3OH conversion at 25 °C following (a) Path 1 - H_2O_2-mediated radical mechanism on the di-oxo center, (b) Path 2 - Fenton type mechanism on the mono-oxo center, and (c) Path 3 - CH_4-to-CH_3OOH conversion following H_2O_2-mediated radical mechanism on the di-oxo center. "Fe" on the profiles stands for the FeN_4/GN catalyst structure, and "TS" represents the transition state. Asterisk (*) denotes the adsorbed species on the catalyst surface. Selected interatomic distances (in Å) are shown on the molecular structures.

Table 2 Steady-state net reaction rates of all elementary steps in the reduced set of the reaction mechanisms calculated by MKM at 25 °C and reaction conditions tabulated in Table 1.

	Elementary step†	Step††	Rate (s^{-1})‡	Starting state	Ending state	Pathway
R1	$FeO_2 + CH_4 \rightarrow FeO_2 + CH_4$*	Ads	1.70E-07	1	2	1, 3
R2	$FeO_2 + CH_4$* $\rightarrow$ OFeOH + CH_3·*	TS1	1.70E-07	2	3	1, 3
R3	OFeOH + CH_3·* + H_2O_2 $\rightarrow$ OFeOH + CH_3·* + H_2O_2*	Ads	1.47E-06	3	4	1, 3
R4	OFeOH + CH_3·* + H_2O_2* $\rightarrow$ OFeOH + CH_3OH* + OH·*	TS2	1.75E-07	4	5	1
R5	OFeOH + CH_3OH* + OH·* $\rightarrow$ OFeOH + CH_3OH + OH·*	Des	1.75E-07	5	6	1
R6	OFeOH + OH·* $\rightarrow$ FeO_2 + H_2O*	TS3	1.70E-07	6	7	1, 3
R7	FeO_2 + H_2O* $\rightarrow$ FeO_2 + H_2O	Des	1.70E-07	7	1	1, 3
R8	FeO + H_2O_2 $\rightarrow$ OFe + H_2O_2*	Ads	1.39E-06	8	9	2
R9	OFe + H_2O_2* + CH_4 $\rightarrow$ OFe + H_2O_2* + CH_4*	Ads	1.39E-06	9	10	2
R10	OFe + H_2O_2* + CH_4* $\rightarrow$ OFeOH + OH·* + CH_4*	TS4	1.39E-06	10	11	2
R11	OFeOH + OH·* + CH_4* $\rightarrow$ OFeOH + H_2O* + CH_3·*	TS5	1.39E-06	11	12	2
R12	OFeOH + H_2O* + CH_3·* $\rightarrow$ OFeOH + H_2O + CH_3·*	Des	1.39E-06	12	3	2
R13	OFeOH + CH_3·* $\rightarrow$ OFe + CH_3OH*	TS6	9.37E-08	3	13	2
R14	OFe + CH_3OH* $\rightarrow$ FeO + CH_3OH	Des	9.37E-08	13	8	2
R15	OFeOH + CH_3·* + H_2O_2* $\rightarrow$ OFe + H_2O* + CH_3OOH*	TS7	1.30E-06	4	14	3
R16	OFe + H_2O* + CH_3OOH* $\rightarrow$ OFe + H_2O* + CH_3OOH	Des	1.30E-06	14	15	3
R17	OFe + H_2O* + H_2O_2 $\rightarrow$ OFe + H_2O* + H_2O_2*	Ads	-5.96E-08	15	16	3
R18	OFe + H_2O* + H_2O_2* $\rightarrow$ OFeOH + OH·* + H_2O*	TS8	-4.96E-09	16	17	3
R19	OFeOH + OH·* + H_2O* $\rightarrow$ OFeOH + OH·* + H_2O	Des	-4.96E-09	17	6	3
R20	OFe + H_2O* $\rightarrow$ FeO	Des	1.30E-06	15	8	2, 3

† Given as forward reactions. Asterisk (*) denotes the adsorbed species on the Fe-center.

†† "Ads" and "Des" represent adsorption and desorption steps, respectively, and "TS#" stands for the transition state involved in the reaction step.

‡ A negative reaction rate indicates that the backward reaction is faster than the forward reaction.

Supplementary Information Section 3). Hence, the reduced model is used in the present work for convenience to analyze the kinetic behaviour. The elementary reactions included in the reduced model are tabulated in Table 2.

Table 2 shows the states and elementary steps that are shared by different reaction pathways. The elementary steps that include different pathways allow for the construction of a nested reaction network, as visualized in Figure 3. The reaction network is composed of the full pathways of paths 1 and 2 and a part of path 3. The rest steps of path 3 (from state 15 to 6) are presented as a dotted line in Figure 3 with the details being omitted due to the net small negative steady-state reaction rates (R17-19 in Table 2). The arrow width indicates magnitude of elementary reaction rates at steady state (Table 2). Figure 3 shows a catalytic cycle with a high TOF that emerges from the construction of the nested network: starting from a mono-oxo center (state 8; upper right), (1) methyl radical is formed following path 2 (from state 8 to 3; blue arrows), (2) CH_3OOH is formed following the steps

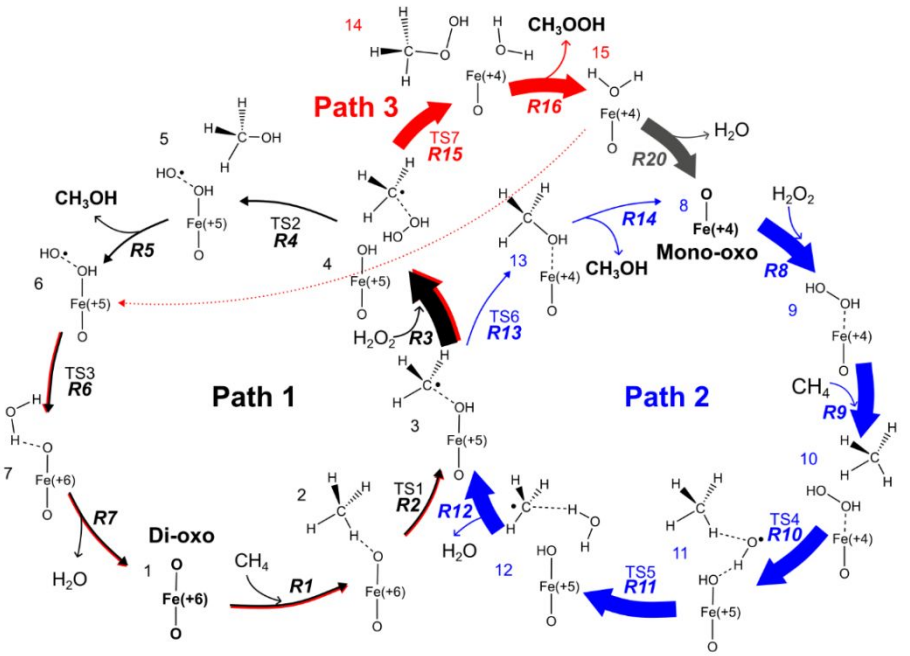

Figure 3 Reaction network of CH_4 conversion to CH_3OH and CH_3OOH. The arrow width indicates the relative steady-state reaction rate of each elementary step estimated by MKM. "Fe" on each structure stands for the FeN_4/GN catalyst with the corresponding formal oxidation state of Fe in parenthesis. The reaction labels correspond to the reactions in Table 2 and the color scheme for each pathway is consistent with Figure 2. Mono-oxo and Di-oxo denote the two different states of the catalyst involved in the catalytic cycles and serve as starting points on the nested reaction network.

identified in path 3 (from state 3 to 15; red arrows), and (3) the mono-oxo center is regenerated as a surface water molecule desorbs (R20). The product of this catalytic cycle is CH_3OOH, with the net reaction being that of rxn.2. In the cycle, the oxidation state of Fe changes between +4 and +5 (Figure 3). CH_3OH can be produced either via a reaction between methyl radical and hydroxyl center (R13 through TS6, i.e., completing path 2) or following the full path 1 from state 4. The latter involves di-oxo catalyst with the high oxidation state of Fe (+6). The Fe oxidation state changes between +4 and +6, as suggested in our previous work.[37]

Figure 4 shows the time evolution of the site distribution and TOFs. The initial di-oxo site (with one H_2O molecule adsorbed; state 7) is gradually converted to mono-oxo (with adsorbates on the bare Fe site: one H_2O molecule - state 15, or both H_2O and H_2O_2 molecules - state 16) over time (Figure 4a). The conversion of the di-oxo state to the mono-oxo state is reasonable given the higher thermodynamic stability of mono-oxo over di-oxo[37] and the high barrier for di-oxo regeneration ($\boldsymbol{\Delta G}^{\ddagger}$ = 1.00 eV; TS8 in Figure 2c). The conversion of di-oxo accelerates after ~10 s and there is a clear switchover from a di-oxo-dominated to a mono-oxo-dominated Fe population at around 50 s. Di-oxo Fe sites have almost completely disappeared at around 400 s.

The TOFs towards both CH_3OH and CH_3OOH production decrease with time: from 5e-6 s^{-1} to 3e-7 s^{-1} for CH_3OH and from 3e-5 s^{-1} to 1.e-6 s^{-1} for CH_3OOH (Figure 4b). The time evolution of the TOFs is linked to the switchover of the site distribution from di-oxo to mono-oxo. Thus, the di-oxo center is more active than the mono-oxo center for both products but is eventually consumed due to the unfavorable thermodynamics and kinetics of its regeneration. The reaction rates of the individual pathways are shown in Figure 4b (TS2, TS6, and TS7 characterize paths 1, 2, and 3, respectively; see Figure 2 for details). The rate of path 3 is identical to the TOF to CH_3OOH as path 3 is the only pathway where CH_3OOH is formed. By contrast, CH_3OH is formed from both paths 1 and 2. The contribution from Path 1 is roughly 2 times of that of Path 2 (Figure 4b).

Four C1 products have been reported experimentally[37]: CH_3OH, CH_3OOH, HCOOH, and $HOCH_2OOH$. Cui et al.[37] proposed that the last two products are produced by oxidation of CH_3OH. However, the possibility of CH_3OOH oxidation to these products cannot be ruled out. Wang et al. demonstrated the room-temperature activity of FeN_4/GN towards C_2H_6 activation, showing that the −OOH derivative (CH_3CH_2OOH) can be further converted to a carboxylic acid (CH_3COOH).[64] A direct comparison of experimental and simulated selectivities is difficult as we do not explore further oxidation of CH_3OH and CH_3OOH. Nevertheless, assuming identical consumption rates of CH_3OH and CH_3OOH (to HCOOH, and $HOCH_2OOH$), the experimental CH_3OH selectivity is 11% (the amount of CH_3OH divided by the amount of CH_3OH + CH_3OOH produced over 10 hours).[37] This is in a good agreement with the MKM-determined CH_3OH selectivity, which is 17% (Figure 4b). It should be noted that the product selectivity is sensitive to the adsorption rate constant ($\boldsymbol{k_a}$). To study the effect of $\boldsymbol{k_a}$, the time evolution of the site distrubution and TOF are simulated with lower and higher adsorption rate constants (Supplementary Information Section 4 and Figure S7). The active site distribution and the total TOF do not depend on $\boldsymbol{k_a}$. However, the CH_3OH selectivity changes to 13% and 29% with 4 times higher and 4 times smaller $\boldsymbol{k_a}$ than the original $\boldsymbol{k_a}$ (eqn. 8), respectively. This result shows a possible relationship between product selectivity and diffusion (see eqn. 6) that is independent of the overall CH_4 conversion by the FeN_4/GN catalyst. The CH_3OH selectivity control strategy by limiting diffusion process has also been suggested by Nørskov et al.[38]

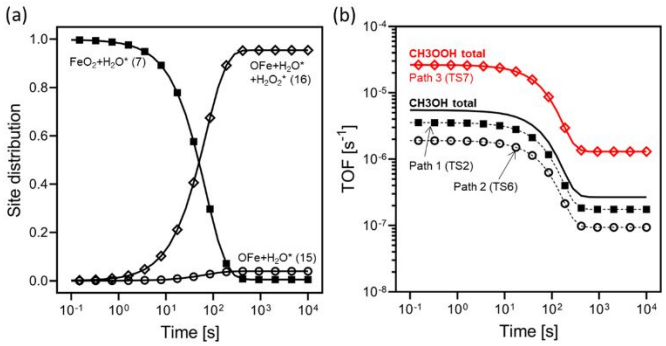

Figure 4 Change of (a) the distribution of the catalytic site and (b) turnover frequency (TOF) over time up to 10^4 s determined by microkinetic modeling (MKM) using a reduced reaction system (paths 1-3) at 25 °C and reaction conditions tabulated in Table 1. On panel (b), the TOF to each product (thick solid lines) is determined as a sum of the rates of the product desorption steps. The TOFs through individual pathways (dotted lines with symbols) represented by reaction rates of their characteristic elementary steps as shown in the parentheses. See Supplementary Information Section 3 for the results with a full reaction system (paths 1-7).

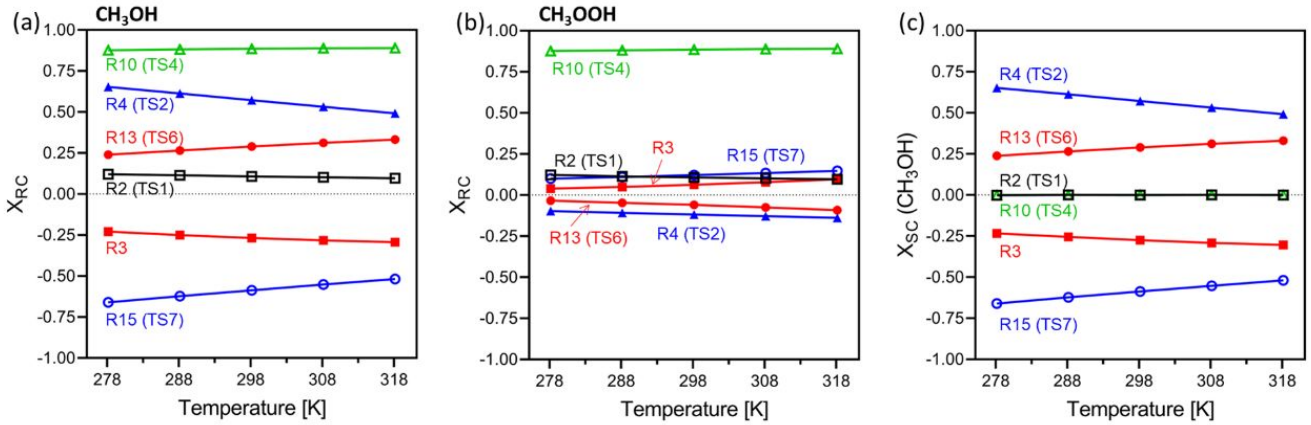

Figure 5 Degree of rate control (X_{RC}) for (a) CH_3OH and (b) CH_3OOH, and (c) degree of selectivity control (X_{SC}) of CH_3OH. The elementary steps that compete are shown with the same color. Details of the elementary steps are found in Table 2. The elementary steps with the absolute value of X_{RC} lower than 2.0e-3 over the studied temperature range are omitted.

Degree of rate and selectivity control. DRC ($X_{RC,i}$) and DSC ($X_{SC,i}$) analyses[60] are shown in Figure 5. For both products, 6 elementary steps are found to have rate control, namely R2, R3, R4, R10, R13, and R15 (Table 2). Among these steps, R10 is found to be the largest rate control with X_{RC} = 0.88-0.89 for both products over the temperature range (278-318 K). R10 is the dissociation of O=O bond in H_2O_2 on the bare Fe side of the mono-oxo center (TS4; see Figure 2b). It has the highest activation energy (0.72 eV) in the most favorable pathway identified in Figure 3 (bold arrows). This step has equivalent influences on both products (CH_3OH and CH_3OOH), and therefore there is no net effect on the product selectivity (i.e., X_{SC} = 0) as seen in Figure 5c. Similarly, R2 has no effect on the selectivity since it has the same effect on both products with a smaller X_{RC} than that of R10 (0.10-0.12). R2 and R10 have no selectivity control since they are associated with the production of states that are shared by both products. As shown in the reaction network in Figure 3, starting from the mono-oxo species (state 8; upper right), the reaction proceeds through a single pathway up to state 3. Hence, all the elementary reaction steps that produce any state between states 8 and 3 have a net zero effect on the product selectivity.

For CH_3OH production, R4 and R15 are equivalently the second most influential steps with similar DRC values but opposite sign (blue lines in Figure 5a): $X_{RC,R4} > 0$ (rate-limiting) and $X_{RC,R15} < 0$ (inhibition). The CH_3OH formation rate is, thus, accelerated and slowed down by increasing the rates of R4 and R15, respectively. They have opposite effects as they occur in parallel at the shared state 4, leading to the production of either CH_3OH (R4) or CH_3OOH (R15) (Figure 3). Thus, the signs of $X_{RC,R4}$ and $X_{RC,R15}$ are exchanged for CH_3OOH compared to CH_3OH (Figure 5b). The magnitudes of X_{RC} of R4 and R15 for CH_3OOH are smaller as the overall TOF to CH_3OOH is much higher than that of CH_3OH (Figure 4b). Consequently, these steps play a significant role in product selectivity (Figure 5c). Similarly, there are two reaction steps that are the third most influential, R3 and R13 (red lines in Figure 5): $X_{RC,R13} > 0$ (rate-limiting) and $X_{RC,R3} < 0$ (inhibition). With increasing temperature (from 278.15 to 318.15 K), R4 and R15 become less influential (smaller absolute values of X_{RC}), whereas R3 and R13 become more influential (larger absolute values of X_{RC}). Hence, all these steps show a significant X_{SC} at a high temperature. Again, the DRC and DSC of these elementary steps (Figure S8) strongly depends on the adsorption rate constant (k_a), primarily because it determines the rate of R3 (H_2O_2 adsorption step). See Supplementary Information Section 4 for further details.

Temperature effect. To understand how the reaction kinetics depend on temperature, we investigate how the TOF changes over time by varying the temperature between 278.15 and 318.15 K as shown in Figure 6. As expected, TOFs to both products increase with temperature. The steady-state TOFs to CH_3OH and CH_3OOH increase by roughly an order of magnitude as the temperature shifts from 298.15 K to 318.15 K. On the other hand, the low-temperature (278.15 K) steady-state TOFs to CH_3OH and CH_3OOH are only 6 and 8% of those at 298.15 K. Interestingly, the TOF to CH_3OH increases more significantly compared to CH_3OOH as temperature increases. This leads to an increase in CH_3OH selectivity with temperature, from 13% (at 278.15 K) to 22% (at 318.15 K) (see Figure 5c). This clearly demonstrates that temperature not only modifies the overall reaction rate but also controls product selectivity, where a small increase in temperature leads to higher TOF to CH_4 and higher selectivity toward CH_3OH. Nevertheless, it should be noted that an increase in temperature can also potentially lead to over-oxidation to CO_2, which cannot be assessed in the present model.

Apparent activation energy and reaction order analysis. Based on the temperature dependent steady-state TOFs to CH_3OH and CH_3OOH (Figure 6a and b), we produce the Arrhenius plots shown in Figure 7a. In the given temperature range, the apparent activation energies ($\Delta E_{app.}^{\ddagger}$) for CH_3OH and CH_3OOH are 1.06 and 0.94 eV, respectively. The apparent activation energy can also be calculated from the degree of rate control and relative Gibbs free energies of each step as reported by Mao and Campbell.[65] Considering only the 6 elementary steps

reported in Figure 5 with an ideal behavior assumption (i.e., neglecting effects of adsorbing/desorbing species and catalytic site fractions), $\Delta E^{\ddagger}_{app.}$ = 1.07-1.09 eV for CH_3OH and 0.88-0.84 eV for CH_3OOH, which are increasing and decreasing with temperature (from 278.15 to 318.15 K), respectively. Both results agree with the higher TOF of CH_3OOH than that of CH_3OH reported in Figure 4.

effect on the overall activity (nearly constant $\Delta E^{\ddagger}_{app.}$) but significantly affects $n_{H_2O_2}$ in such a way that the lower k_a results to higher magnitude of $n_{H_2O_2}$. The selectivity control by $[H_2O_2]$ can, thus, be facilitated by slowing down the diffusion. In addition, as already mentioned, the CH_3OH selectivity increases with temperature (Figure 6c). Taken all together, we demonstrate the synergistic effects among temperature, $[H_2O_2]$, and diffusion

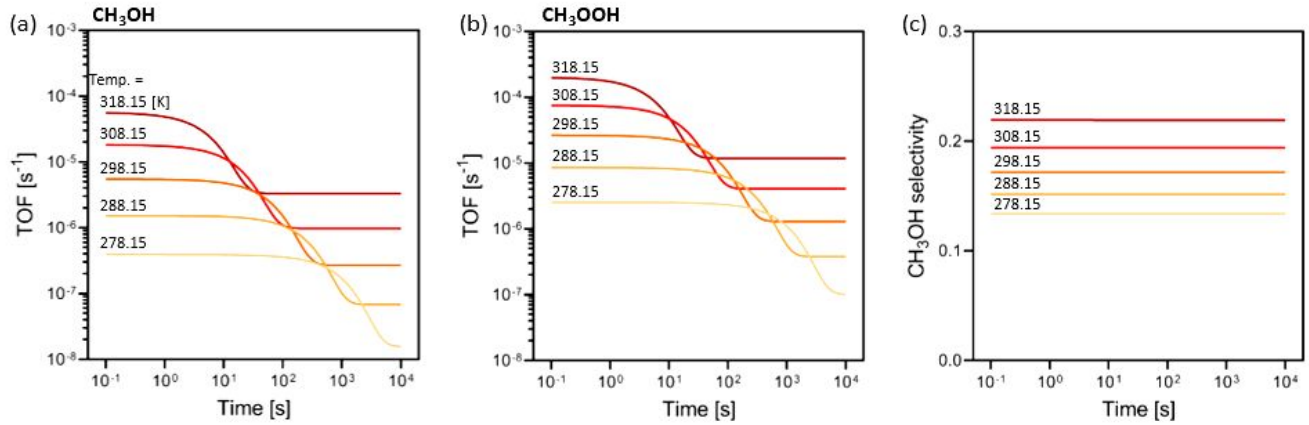

Figure 6 TOFs to (a) CH_3OH and (b) CH_3OOH, and (c) CH_3OH selectivity under various temperatures between 278.15 and 318.15 K over time up to 10^4 s.

The reaction orders, n_i, of the reactants (CH_4 and H_2O_2) with respect to each product (CH_3OH and CH_3OOH) obtained by eqn. 13 are presented in Figure 7b. Reaction rates of both products depend linearly on $[CH_4]$ over the temperature range investigated (i.e., n_{CH_4}= 1). On the contrary, $n_{H_2O_2}$ is smaller for both products; around -0.23 for CH_3OH and 0.06-0.19 for CH_3OOH and increasing with temperature. Thus, increased $[H_2O_2]$ yields slower CH_3OH formation and faster CH_3OOH formation. The reason for the different signs of the H_2O_2 reaction order is that R3 (H_2O_2 adsorption) outcompetes the parallel reaction, R13 (see Figure 3). Although the rate of the minor reaction stream to form CH_3OH after state 4 increases as the rate of R3 increases, the decrease in the rate of R13 counteracts this effect, leading to a net decrease in CH_3OH formation rate. Thus, the product selectivity can be controlled by modifying $[H_2O_2]$, where low $[H_2O_2]$ favors high CH_3OH selectivity.

It is worth noting that the difference between $n_{H_2O_2}$ for the two products increases with temperature. This indicates that selectivity control by $[H_2O_2]$ is more significant at a higher temperature, as also seen in Figure 5c (red lines; R3 is adsorption of H_2O_2 from bulk phase to catalyst).

The apparent activation energies and reaction orders have been also investigated with different adsorption rate constants (k_a) (Figure S9). The analysis shows that varying k_a has a small

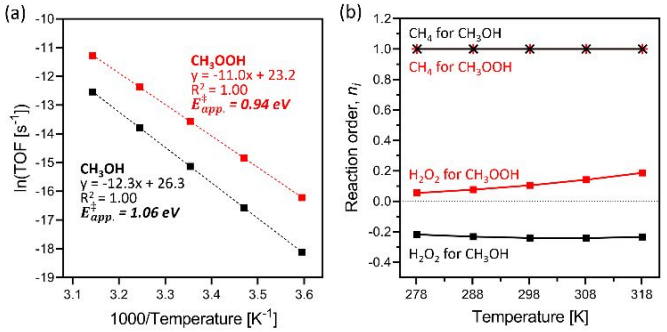

Figure 7 (a) Arrhenius plots for the production of CH_3OH (black) and CH_3OOH (red) with linear fits and apparent activation energies ($E^{\ddagger}_{app.}$). (b) Reaction order of reactants (CH_4 and H_2O_2) for each product.

on controlling product selectivity, where the CH_3OH selectivity can be enhanced by reaction conditions with high temperature, low $[H_2O_2]$, and slow diffusion. This provides a large design space for room-temperature CH_4 conversion by a FeN_4/GN catalyst towards target liquid product.

Conclusions

We developed a first-principles-based mean-field microkinetic model (MKM) for partial CH_4 conversion to CH_3OH and CH_3OOH over FeN_4/GN. In total, 7 reaction mechanisms (5 for CH_3OH and 2 for CH_3OOH) on two different Fe-centers (i.e., di-oxo and mono-oxo) are considered. A reaction network is constructed, which involves a dynamic change of the Fe oxidation state between +4, +5 and +6. The evolution of the site fraction shows that the di-oxo site is converted to the mono-oxo site over time. The switchover from di-oxo to mono-oxo is connected to a significant drop in turnover frequency (TOF). Thus, the di-oxo center (Fe^{+6}) is more active but less stable compared to the mono-oxo center (Fe^{+4}). The catalytic activity for CH_3OH formation can, therefore, be enhanced by stabilizing the metal center in the di-oxo form. CH_3OH and CH_3OOH are found to be minor and major reaction products, respectively. The CH_3OH selectivity is found to be 17%, which agrees with the experimental observations.[37] The degree of rate control analysis shows that scission of the O=O bond in H_2O_2 is rate-controlling. Interestingly, however, this step has no net effect on product selectivity. Instead, two pairs of competing elementary reaction steps with significant influences on the product selectivity are identified by the degree of selectivity analysis. The apparent activation energies obtained from Arrhenius plots are consistent with the fact that CH_3OOH is the major product. The apparent

activation energy for CH_3OOH is calculated to be 0.94 eV, whereas the value is 1.06 eV for CH_3OH.

Three key factors for product selectivity control are identified: temperature, H_2O_2 concentration, and diffusion. Increasing temperature accelerates the overall TOF as expected. As the CH_3OH formation rate has a stronger temperature dependence than CH_3OOH formation, the CH_3OH selectivity can be enhanced by increasing the temperature. The reaction order analysis demonstrates the opposite effect of $[H_2O_2]$ on the product distribution. The CH_3OH production is favored by a lower $[H_2O_2]$. Furthermore, the diffusion of free species from bulk phase to a catalyst surface is found to play a significant role in the reaction kinetics by altering product selectivity without affecting the overall CH_4 conversion. More importantly, we reveal that there is a synergistic effect among these factors as they have a mutual dependence. This suggests a significant engineering space exists for product selectivity in CH_4 conversion by FeN_4/GN catalyst.

Generally, we demonstrated that the DFT-based kinetic modeling is a useful tool for investigating complicated reaction systems like that of methane to methanol conversion. Our findings provide an in-depth kinetic understanding of the low-temperature CH_4 conversion to C1 products, which can potentially guide experimental efforts to discover efficient catalysts, as well as fine-tune catalytic performance.

Author Contributions

The project was conceptualized and supervised by G.M. and H.G. Computational chemistry calculations were performed by S.H. Microkinetic modeling was performed by M.M.K. and S.H. in cooperation with E.V.M. The original draft of the manuscript was prepared by S.H., M.M.K., G.M. and H.G. All authors contributed to scientific discussions and editing of the manuscript.

Conflicts of interest

There are no conflicts to declare.

Acknowledgements

This material is based upon work supported by the National Science Foundation (NSF) under Grant No. 1920623. GM acknowledges sabbatical support from Chalmers University of Technology, Areas of Advance: Materials Science, and the Wenner Gren Foundation. M.M.K and H.G. acknowledge support from the Knut and Alice Wallenberg Foundation (KAW 2015.0058) and the Swedish Research Council (2020-05191). The Competence Centre for Catalysis (KCK) is hosted by Chalmers University of Technology and financially supported by the Swedish Energy Agency and the member companies Johnson Matthey, Perstorp, Powercell, Preem, Scania CV, Umicore and Volvo Group. This research was supported in part by the University of Pittsburgh Center for Research Computing, RRID:SCR_022735, through the resources provided. Specifically, this work used the H2P cluster, which is supported by NSF award number OAC-2117681.

References

1 BP Statistical Review of World Energy 2021, BP p.l.c., London, 2021.
2 Carbon Dioxide Emissions Coefficients by Fuel, U.S. Energy Information Administration, https://www.eia.gov/environment/emissions/co2_vol_mass.php (accessed April 2023).
3 A. Moumen, G. Azizi, K. B. Chekroun and M. Baghour, *International Journal of Global Warming*, 2016, 9(2), 229-253.
4 2023 Global Gas Flaring Tracker Report, Global Gas Flaring Reduction Partnership, Washington, DC: World Bank Publications, https://thedocs.worldbank.org/en/doc/5d5c5c8b0f451b472e858ceb97624a18-0400072023/original/2023-Global-Gas-Flaring-Tracker-Report.pdf (accessed April 2023).
5 A. P. E. York, T. Xiao and M. L. H. Green, *Topics in Catalysis*, 2003, 22(3-4), 345-358.
6 H. D. Gesser, N. R. Hunter and C. B. Prakash, *Chemical Reviews*, 1985, 85(4), 235-244.
7 J. R. Rostrup-Nielsen, J. Sehested and J. K. Nørskov, *Advances in Catalysis*, 2002, 47, 65-139.
8 S. Verhelst, J. W. G. Turner, L. Sileghem and J. Vancoillie, *Progress in Energy and Combustion Science*, 2019, 70, 43-88.
9 A. Hamnett, *Catalysis Today*, 1997, 38(4), 445-457.
10 S. Wasmus and A. Küver, *Journal of Electroanalytical Chemistry*, 1999, 461(1-2), 14-31.
11 G. J. Hatchings, C. P. Nicolaides and M. S. Scurrell, Catalysis Today, 1992, 15(1), 23-49.
12 F. Yaripour, F. Baghaei, I. Schmidt and J. Perregaard, *Catalysis Communications*, 2005, 6(2), 147-152.
13 T. Waters, R. A. J. O'Hair and A. G. Wedd, *Journal of the American Chemical Society*, 2003, 125(11), 3384-3396.
14 M. Ravi, M. Ranocchiari and J. A. van Bokhoven, *Angewandte Chemie International Edition*, 2017, 56(52), 16464-16483.
15 R. H. Crabtree, *Chemical Reviews*, 1995, 95, 987-1007.
16 P. Kumar, T. A. Al-Attas, J. Hu and M. G. Kibria, *ACS Nano*, 2022, 16(6), 8557-8618.
17 N. Aristov and P. B. Armentrout, *Journal of Physical Chemistry*, 1987, 91, 6178-6188.
18 Y.-M. Chen, D. E. Clemmer and P. B. Armentrout, *Journal of the American Chemical Society*, 1994, 116, 7815-7826.
19 D. Schröder, H. Schwarz, D. E. Clemmer, Y. Chen, P. B. Armentrout, V. I. Baranov and D. K. Böhme, *International Journal of Mass Spectrometry and Ion Processes,* 1997, 161(1-3), 175-191.
20 A. E. Shilov and G. B. Shul'pin, *Chemical Reviews*, 1997, 97(8), 2879-2932.
21 S. Shaik, D. Danovich, A. Fiedler, D. Schröder and H. Schwarz, *Helvetica Chimica Acta*, 1995, 78(6), 1393-1407.
22 K. Yoshizawa, Y. Shiota and T. Yamabe, *The Journal of Chemical Physics*, 1999, 111, 538-545.
23 E. E. Claveau, S. Sader, B. A. Jackson, S. N. Khan and E. Miliordos, *Physical Chemistry Chemical Physics*, 2023, 25, 5313-5326.
24 R. A. Periana, D. J. Taube, E. R. Evitt, D. G. Löffler, P. R.

Wentrcek, G. Voss and T. Masuda, *Science*, 1993, 259(5093), 340-343.
25 R. A. Periana, D. J. Taube, S. Gamble, H. Taube, T. Satoh and H. Fujii, *Science*, 1998, 280(5363), 560-564.
26 H. Dalton, *Catalysis Today*, 1992, 13(2-3), 455-461.
27 J. D. Lipscomb, *Annual Review of Microbiology*, 1994, 48, 371-399.
28 M.-H. Baik, M. Newcomb, R. A. Friesner and S. J. Lippard, *Chemical Reviews*, 2003, 103(6), 2385-2420.
29 S. Sirajuddin and A. C. Rosenzweig, *Biochemistry*, 2015, 54(14), 2283-2294.
30 K. A. Dubkov, V. I. Sobolev, E. P. Talsi, M. A. Rodkin, N. H. Watkins, A. A. Shteinman and G. I. Panov, *Journal of Molecular Catalysis A: Chemical*, 1997, 123(2-3), 155-161.
31 G. I. Panov, A. K. Uriarte, M. A. Rodkin and V. I. Sobolev, *Catalysis Today*, 1998, 41(4), 365-385.
32 E. V. Starokon, M. V. Parfenov, S. S. Arzumanov, L. V. Pirutko, A. G. Stepanov and G. I. Panov, *Journal of Catalysis*, 2013, 300, 47-54.
33 M. H. Groothaert, P. J. Smeets, B. F. Sels, P. A. Jacobs and R. A. Schoonheydt, *Journal of the American Chemical Society*, 2005, 127(5), 1394-1395.
34 H. A. Doan, Z. Li, O. K. Farha, J. T. Hupp and R. Q. Snurr, *Catalysis Today*, 2018, 312, 2-9.
35 S. Grundner, M. A. C. Markovits, G. Li, M. Tromp, E. A. Pidko, E. J. M. Hensen, A. Jentys, M. Sanchez-Sanchez and J. A. Lercher, *Nature Communications*, 2015, 6, 7546.
36 M. V. Parfenov, E. V. Starokon, L. V. Pirutko and G. I. Panov, *Journal of Catalysis*, 2014, 318, 14-21.
37 X. Cui, H. Li, Y. Wang, Y. Hu, L. Hua, H. Li, X. Han, Q. Liu, F. Yang, L. He, X. Chen, Q. Li, J. Xiao, D. Deng and X. Bao, *Chem*, 2018, 4, 1902-1910.
38 A. A. Latimer, A. Kakekhani, A. R. Kulkarni and J. K. Nørskov, *ACS Catalysis*, 2018, 8(8), 6894-6907.
39 C. Hammond, M. M. Forde, M. H. Ab Rahim, A. Thetford, Q. He, R. L. Jenkins, N. Dimitratos, J. A. Lopez-Sanchez, N. F. Dummer, D. M. Murphy, A. F. Carley, S. H. Taylor, D. J. Willock, E. E. Stangland, J. Kang, H. Hagen, C. J. Kiely and G. J. Hutchings, *Angewandte Chemie International Edition*, 2012, 51(21), 5129-5133.
40 S. Hong and G. Mpourmpakis, *Catalysis Science & Technology*, 2021, 11, 6390-6400.
41 S. Kozuch and S. Shaik, *Accounts of Chemical Research*, 2011, 44(2), 101-110.
42 C. V. Ovesen, B. S. Clausen, B. S. Hammershøi, G. Steffensen, T. Askgaard, I. Chorkendorff, J. K. Nørskov, P. B. Rasmussen, P. Stoltze and P. Taylor, *Journal of Catalysis*, 1996, 158(1), 170-180.
43 L. C. Grabow, A. A. Gokhale, S. T. Evans, J. A. Dumesic and M. Mavrikakis, *The Journal of Physical Chemistry C*, 2008, 112(12), 4608-4617.
44 K. Reuter, *Catalysis Letters*, 2016, 146, 541-563.
45 M. M. Kauppinen, M. M. Melander, A. S. Bazhenov and K. Honkala, *ACS Catalysis*, 2018, 8(12), 11633-11647.
46 A. H. Motagamwala and J. A. Dumesic, *Chemical Reviews*, 2020, 121(2), 1049-1076.
47 Y. Feng, X. Wang, T. V. W. Janssens, P. N. R. Vennestrøm, J. Jansson, M. Skoglundh and H. Grönbeck, *ACS Catalysis*, 2021, 11(23), 14395-14407.
48 M. Kauppinen, A. Posada-Borbon and H. Grönbeck, *The Journal of Physical Chemistry C*, 2022, 126(36), 15235-15246.
49 M. Abdelgaid, E. V. Miu, H. Kwon, M. M. Kauppinen, H. Grönbeck and G. Mpourmpakis, *Catalysis Science & Technology*, 2023, 13, 3527-3536.
50 M. J. Frisch, G. W. Trucks, H. B. Schlegel, G. E. Scuseria, M. A. Robb, J. R. Cheeseman, G. Scalmani, V. Barone, B. Mennucci, G. A. Petersson, H. Nakatsuji, M. Caricato, X. Li, H. P. Hratchian, A. F. Izmaylov, J. Bloino, G. Zheng, J. L. Sonnenberg, M. Hada, M. Ehara, K. Toyota, R. Fukuda, J. Hasegawa, M. Ishida, T. Nakajima, Y. Honda, O. Kitao, H. Nakai, T. Vreven, J. A. M. Jr., J. E. Peralta, F. Ogliaro, M. Bearpark, J. J. Heyd, E. Brothers, K. N. Kudin, V. N. Staroverov, R. Kobayashi, J. Normand, K. Raghavachari, A. Rendell, J. C. Burant, S. S. Iyengar, J. Tomasi, M. Cossi, N. Rega, J. M. Millam, M. Klene, J. E. Knox, J. B. Cross, V. Bakken, C. Adamo, J. Jaramillo, R. Gomperts, R. E. Stratmann, O. Yazyev, A. J. Austin, R. Cammi, C. Pomelli, J. W. Ochterski, R. L. Martin, K. Morokuma, V. G. Zakrzewski, G. A. Voth, P. Salvador, J. J. Dannenberg, S. Dapprich, A. D. Daniels, O. Farkas, J. B. Foresman, J. V. Ortiz, J. Cioslowski and D. J. Fox, 2014, Gaussian 09 (Revision D.01), Gaussian Inc., Wallingford, CT.
51 A. D. Becke, *The Journal of Chemical Physics*, 1992, 96, 2155-2160.
52 C. Lee, W. Yang and R. G. Parr, *Physical Review B*, 1988, 37, 785.
53 C. Gonzalez and H. B. Schlegel, *The Journal of Chemical Physics*, 1989, 90, 2154-2161.
54 V. Barone and M. Cossi, *The Journal of Physical Chemistry A*, 1998, 102(11), 1995-2001.
55 R. A. Alberty, *The Journal of Chemical Thermodynamics*, 2006, 38(4), 396-404.
56 O. J. Conquest, T. Roman, A. Marianov, A. Kochubei, Y. Jiang and C. Stampfl, *Journal of Chemical Theory and Computation*, 2021, 17(12), 7753-7771.
57 N. L. Haworth, Q. Wang and M. L. Coote, *The Journal of Physical Chemistry A*, 2017, 121(27), 5217-5225.
58 Y. Saito, *Review of Polarography*, 1968, 15(6), 177-187.
59 P. Virtanen, R. Gommers, T. E. Oliphant, M. Haberland, T. Reddy, D. Cournapeau, E. Burovski, P. Peterson, W. Weckesser, J. Bright, S. J. van der Walt, M. Brett, J. Wilson, K. J. Millman, N. Mayorov, A. R. J. Nelson, E. Jones, R. Kern, E. Larson, C. J. Carey, İ. Polat, Y. Feng, E. W. Moore, J. VanderPlas, D. Laxalde, J. Perktold, R. Cimrman, I. Henriksen, E. A. Quintero, C. R. Harris, A. M. Archibald, A. H. Ribeiro, F. Pedregosa, P. van Mulbregt and SciPy 1.0 Contributors, *Nature Methods*, 2020, 17, 261-272.
60 C. T. Campbell, *ACS Catalysis*, 2017, 7(4), 2770-2779.
61 J. Kestin, M. Sokolov and W. A. Wakeham, *Journal of Physical and Chemical Reference Data*, 1978, 7, 941-948.
62 Z. Duan and S. Mao, *Geochimica et Cosmochimica Acta*, 2006, 70(13), 3369-3386.
63 S. Sun, N. F. Dummer, T. Bere, A. J. Barnes, G. Shaw, M. Douthwaite, S. Pattisson, R. J. Lewis, N. Richards, D. J. Morgan and G. J. Hutchings, *Catalysis Science & Technology*, 2022, 12, 3727-3736.
64 S. Wang, H. Li, M. He, X. Cui, L. Hua, H. Li, J. Xiao, L. Yu, N. P. Rajan, Z. Xie and D. Deng, *Journal of Energy Chemistry*, 2019, 36, 47-50.
65 Z. Mao and C. T. Campbell, *ACS Catalysis*, 2019, 9(10), 9465-9473.